Excitonic instability in transition metal dichalcogenides

OPEN ACCESS
IOP Publishing
Journal of Physics: Condensed Matter
J. Phys.: Condens. Matter **34** (2022) 455303 (8pp)
https://doi.org/10.1088/1361-648X/ac8f7d

Excitonic instability in transition metal dichalcogenides

M F C Martins Quintela[1,2,*], A T Costa[2] and N M R Peres[1,2]

[1] Department of Physics and Centre of Physics of the Universites of Minho and Porto (CF–UM–UP), Campus of Gualtar, 4710-057 Braga, Portugal
[2] International Iberian Nanotechnology Laboratory (INL), Av. Mestre José Veiga, 4715-330 Braga, Portugal

E-mail: mfcmquintela@gmail.com

Received 7 June 2022, revised 9 August 2022
Accepted for publication 5 September 2022
Published 14 September 2022

Abstract

When transition-metal dichalcogenide monolayers lack inversion symmetry, their low-energy single particle spectrum near some high-symmetry points can, in some cases, be described by tilted massive Dirac Hamiltonians. The so-called Janus materials fall into that category. Inversion symmetry can also be broken by the application of out-of-plane electric fields, or by the mere presence of a substrate. Here we explore the properties of excitons in TMDC monolayers lacking inversion symmetry. We find that exciton binding energies can be larger than the electronic band gap, making such materials promising candidates to host the elusive exciton insulator phase. We also investigate the excitonic contribution to their optical conductivity and discuss the associated optical selection rules.

Keywords: Janus, TMD, exciton, monolayer, conductivity, tilted Dirac cone

(Some figures may appear in colour only in the online journal)

1. Introduction

Janus transition metal dichalcogenide (TMD) monolayers are a new type of two–dimensional materials, recently synthesized [1, 2] in the form of MoSSe. In this material, one atomic layer of Mo is encapsulated by two different chalcogen layers, namely S and Se. This creates an asymmetry in the direction perpendicular to the plane of the structure, resulting in a dipole moment pointing from the Se to the S layer [3, 4]. These first two independent experiments [1, 2] triggered a large wave of theoretical studies [5] into the electronic band structure [2], anisotropic elasticity and transport [6], as well as piezoelectric [7], pyroelectric [8], spin [9], and photocarrier [10] properties of Janus structures. Additionally, several potential applications have been studied, such as in water splitting [11], gas sensing [12], and photovoltaics [13].

The band structure and the Berry curvature dipole [14–16] of Janus TMD monolayers are well described by a tilted massive Dirac model [17–19]. For instance, this two-band effective model captures the pronounced peak in the dipole component near the Fermi level of T′ – WSTe, seen in DFT calculations [17]. This feature is a consequence of a reduced band gap, which leads to a large Berry curvature [17]. Tilted Dirac cones are also seen in 8-*Pmmm* borophene [20–22], where the low-energy regime near the Dirac points can be accurately described via an effective anisotropic tilted Hamiltonian [20, 21, 23, 24].

Several properties of systems with tilted massive Dirac Hamiltonians have been studied, such as anomalous spin transport [25], topological properties [26], photoinduced anomalous [27] and nonlinear Hall effects [18], quantum criticality [28], chiral excitonic instabilities [29], and orbital-selective

* Author to whom any correspondence should be addressed.

photoexcitation [30]. Additionally, the importance of spin–orbit coupling in layered organic salts has also been studied via a Hamiltonian with tilted band structure [31, 32]. Explicit inversion symmetry breaking and anisotropic terms are also present in other families of materials, such as Weyl semimetals [33] with broken tilt inversion symmetry, where second harmonic generation has been recently studied [34], and type-II semi-Dirac semimetals [35–37], where it has been shown that linear and nonlinear anomalous Hall effects can be manipulated via circularly polarized light [38].

A defining feature of massive tilted Dirac cones is the tunability of their electronic band gap, illustrated in figure 1. By tuning a single parameter, it is possible to go from a direct gap semiconductor to a metal, passing through an indirect gap semiconductor and a semi-metal. *Ab initio* calculations [39] suggest that such tunability can be achieved in real materials by the application of an out-of-plane electric field. Thus, materials that host massive tilted Dirac cones are especially attractive as platforms on which new electronic phases can be found. One such phase is the excitonic insulator, first predicted qualitatively by Mott [40]. The concept has been subsequently refined and put on firmer grounds by several authors [41–44]. In brief, when the binding energy of excitons surpasses the value of the electronic band gap, the system becomes unstable against a proliferation of excitons [45]. The true ground state of such a system is an 'exciton condensate', akin in many ways to the Cooper pair condensate found in superconductors [43]. This analysis applies equally to small gap semiconductors and semimetals, provided the overlap between conduction and valence bands is small, such that screening of the Coulomb interaction between electrons and holes is negligible. Although predicted more than 60 years ago, the excitonic insulator has eluded conclusive experimental observation until very recently [46–50]. One of the main difficulties is that the excitonic instability is frequently accompanied by structural instabilities, associated with the softening of phonon modes, which are hard to disentangle from the former.

Here we look into the properties of excitons in 2D massive tilted Dirac electrons. We show that the band gap can be tuned while the exciton binding energy remains constant, moving the system towards an excitonic instability. Importantly, as the magnitude of the gap decreases, the maximum of the valence band and the minimum of the conduction band shift in opposite directions in reciprocal space, making the gap indirect. This guarantees that the dielectric function of the material remains finite even as the gap approaches zero, and the exciton binding energies are not strongly affected by the smallness of the gap [41]. It is also noteworthy that the excitonic contribution to the conductivity is insensitive to the tilting parameter; thus, at least in principle, one can expect a sudden change in transport properties as the excitonic instability is reached by tuning of the tilting parameter.

This paper is structured as follows. In section 2, we discuss the tilted Dirac Hamiltonian [18], illustrating the features induced by the tilt parameter on the single particle electronic eigenstates and band structure. In section 3, we introduce the Bethe–Salpeter equation, briefly discussing the electrostatic potential coupling different bands. The screening length of the material is also introduced, and the influence of the tilt parameter on the excitonic states is analyzed. Finally, the optical selection rules and oscillator strengths are discussed, and the excitonic optical conductivity is computed.

2. Tilted Dirac Hamiltonian

The effective two-band tilted Dirac Hamiltonian has been shown to capture the essential features of both the low-energy band structure and the Berry curvature dipole moment of Janus TMD monolayers, such as WSTe [17]. This Hamiltonian includes an anisotropic term which preserves time-reversal symmetry but explicitly breaks inversion symmetry, tilting the band structure in a specific direction, here considered to be the x-axis. The Hamiltonian can therefore be written as [16–18]

$$\hat{\mathcal{H}}_d = tk^x\sigma_0 + v\left(k^y\sigma_x + \eta k^x\sigma_y\right) + \left(m/2 - \alpha k^2\right)\sigma_z, \qquad (1)$$

where (k_x, k_y) are the wave vectors, $k^2 = k_x^2 + k_y^2$, $(\sigma_x, \sigma_y, \sigma_z)$ are the Pauli matrices, σ_0 is the 2×2 identity matrix, $\eta = \pm 1$ is a valley–like index, m is the gap, and t tilts the Hamiltonian in the x direction. In equation (1), the α parameter is introduced to regulate topological properties as $k \to \infty$ [51]. For clarity, we also write this Hamiltonian in matrix form, where it is given by

$$\hat{\mathcal{H}}_d = \begin{bmatrix} tk_x + \left(\frac{m}{2} - \alpha k^2\right) & -iv\left(\eta k_x + ik_y\right) \\ iv\left(\eta k_x - ik_y\right) & tk_x - \left(\frac{m}{2} - \alpha k^2\right) \end{bmatrix}. \qquad (2)$$

The band dispersion of this model is given by

$$E_\lambda(k) = tk_x + \lambda\sqrt{k^2v^2 + \left(m/2 - \alpha k^2\right)^2}, \qquad (3)$$

with $\lambda = \pm 1$ the conduction/valence band index. Choosing $\eta = -1$ as in [17, 18], the (non-normalized) eigenvectors are given by

$$|u_+(k,\theta)\rangle = \begin{bmatrix} i\frac{m - 2\alpha k^2 + \lambda\sqrt{k^2v^2 + (m/2 - \alpha k^2)^2}}{2kv} \\ e^{i\theta} \end{bmatrix},$$
$$|u_-(k,\theta)\rangle = \begin{bmatrix} ie^{-i\theta}\frac{m - 2\alpha k^2 + \lambda\sqrt{k^2v^2 + (m/2 - \alpha k^2)^2}}{2kv} \\ 1 \end{bmatrix}, \qquad (4)$$

where $\theta = \arctan(k_y/k_x)$. By inspection of both equations (3) and (4) it is immediately clear that the tilt parameter t influences neither the difference between the two bands (i.e. $E_+(k) - E_-(k)$) nor the eigenstates of the Hamiltonian. Its only effect is to produce a tilt of the dispersion relation along the x-axis. In figure 1 we show the dispersion relation for a few representative values of t. The other parameters have been chosen as $v = 1\,\text{eV Å}$, $\alpha = 1\,\text{eV Å}^2$ and $m = 0.2\,\text{eV}$ [18]. For $t = 0$ (top left) there is a gap at $k = 0$, which is continuously suppressed as $t \to v$. Notice also that, for any $0 < t < v$, the gap becomes indirect. For $t/v \geqslant 1$ (bottom panels) the model describes a semimetal with zero ($t = v$) or small $t/v \gtrsim 1$ carrier density.

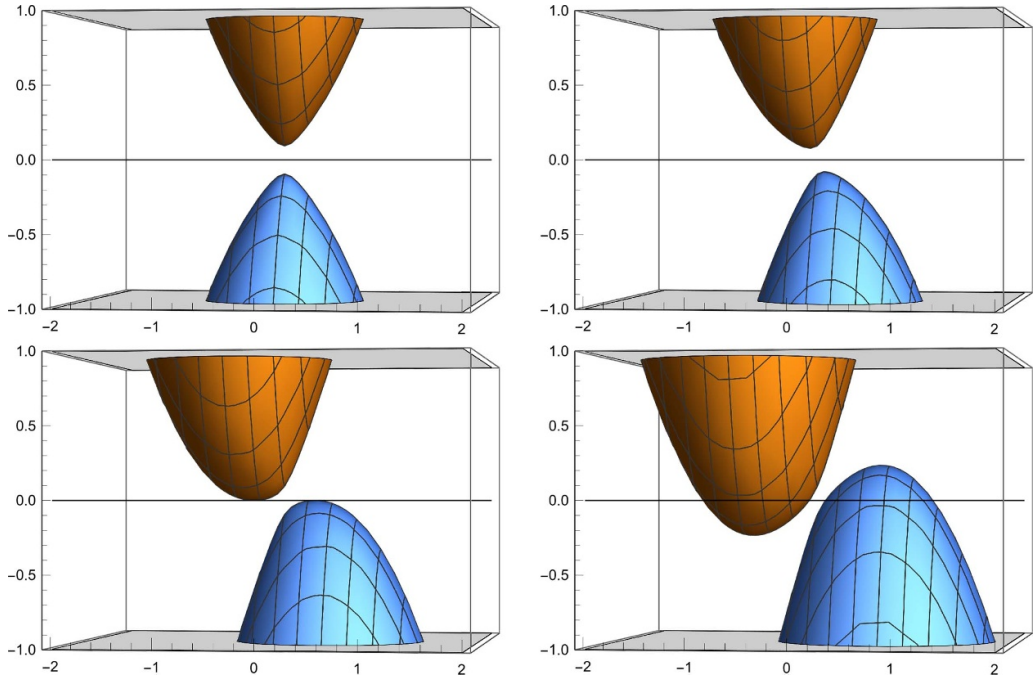

Figure 1. 3D plot of the band structure of the tilted Dirac Hamiltonian of equation (1) for $t/v = 0$ (top-left), $t/v = 0.5$ (top-right), $t/v = 1$ (bottom-left), and $t/v = 1.5$ (bottom-right). Labeled axes are the k_x axis (horizontal, in Å^{-1}) and energy (vertical, in eV).

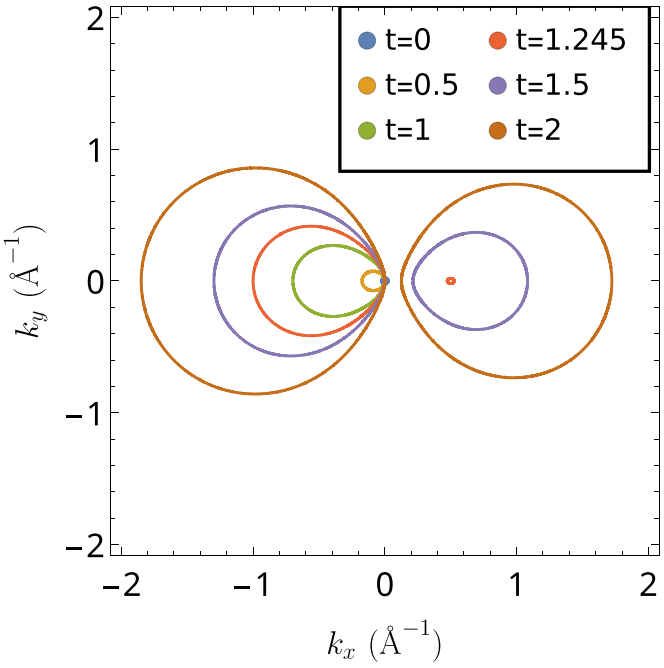

Figure 2. Fermi rings of the Hamiltonian of equation (1) at $E_F = m/2$ for various values of t/v. The rings associated with the conduction band are present on the left of the figure, while those associated with the valence bands are present on the right.

In figure 2, we plot the Fermi rings at a Fermi energy of $E_F = m/2$ for various values of t/v. The top of the valence band crosses the $E = \dfrac{m}{2}$ plane at roughly $t/v \approx 1.245$, as can be seen from the sudden appearance of the Fermi ring regarding this band. The anisotropy introduced by the tilt of the bands along the k_x axis is also clear when compared with the full symmetry along the k_y axis.

3. Excitons in tilted Dirac materials

We now look at the excitons of the massive tilted Dirac fermion model. Our approach is to solve the Bethe–Salpeter equation (BSE). As neither the difference between the two bands nor the eigenvectors depend on t, we do not expect this parameter to play a part in the excitonic properties of the system.

3.1. Solving the Bethe–Salpeter equation

The Bethe–Salpeter equation can be written in momentum space as [52–55]

$$E\,\psi_{c;v}(\mathbf{k}) = (E^c_{\mathbf{k}} - E^v_{\mathbf{k}})\,\psi_{c;v}(\mathbf{k}) + \sum_{\mathbf{q}} V(\mathbf{k}-\mathbf{q}) \left\langle u^c_{\mathbf{k}} \mid u^c_{\mathbf{q}} \right\rangle \left\langle u^v_{\mathbf{q}} \mid u^v_{\mathbf{k}} \right\rangle \psi_{c;v}(\mathbf{q}), \quad (5)$$

where $\psi_{c;v}(\mathbf{k})$ is the excitonic wave function that we wish to obtain, $\left|u^{v/c}_{\mathbf{k}}\right\rangle$ and $E^{v/c}_{\mathbf{k}}$ are the single particle electronic wave functions and energies, respectively, and $V(\mathbf{k})$ is an electrostatic potential coupling different bands and thus capturing many-body effects including the intrinsic many-body nature of excitons.

As both the single particle eigenvectors and the direct band gap are independent of the tilt parameter, we assume that the excitons have a well-defined angular momentum ℓ and that we

can write their wave functions as $\psi_{c;v}(\mathbf{k}) = f_{c;v}(k)\, e^{i\ell\theta}$. Under this assumption, we can write the BSE as

$$Ef_{c;v}(k)\, e^{i\ell\theta_k} = (E^c_{\mathbf{k}} - E^v_{\mathbf{k}}) f_{c;v}(k)\, e^{i\ell\theta_k} + \sum_{\mathbf{q}} V(\mathbf{k}-\mathbf{q}) \left\langle u^c_{\mathbf{k}} \mid u^c_{\mathbf{q}} \right\rangle \left\langle u^v_{\mathbf{q}} \mid u^v_{\mathbf{k}} \right\rangle f_{c;v}(q)\, e^{i\ell\theta_q}. \tag{6}$$

Taking the thermodynamic limit and rearranging the complex exponentials, the Bethe–Salpeter equation is now given by

$$Ef_{c;v}(k) = (E^c_{\mathbf{k}} - E^v_{\mathbf{k}}) f_{c;v}(k) - \int \frac{q dq d\theta_q}{4\pi^2} \times \left[V(\mathbf{k}-\mathbf{q}) \left\langle u^c_{\mathbf{k}} \mid u^c_{\mathbf{q}} \right\rangle \left\langle u^v_{\mathbf{q}} \mid u^v_{\mathbf{k}} \right\rangle f_{c;v}(q)\, e^{i\ell(\theta_q - \theta_k)} \right]. \tag{7}$$

The process of solving the Bethe–Salpeter equation in monolayer and multilayer systems has been thoroughly discussed recently [56, 57], so we will not go into the details of the calculations.

We consider the electrostatic interaction to be given by the Rytova–Keldysh potential [58, 59], obtained by solving the Poisson equation for a charge embedded in a thin film of vanishing thickness. In momentum space, this potential is given by

$$V(\mathbf{k}) = 2\pi \frac{\hbar c \alpha}{\epsilon} \frac{1}{k(1 + r_0 k)}, \tag{8}$$

where $\alpha = 1/137$ is the fine-structure constant and ϵ the mean dielectric constant of the medium above/below the monolayer, here considered to be either hexagonal boron-bitride (hBN) or quartz. The parameter r_0 corresponds to an in-plane screening length related to the 2D polarizability of the material. It can be calculated from the single particle Hamiltonian of the system [60], for $t < v$, as

$$r_0 = \frac{\hbar^3 c \alpha}{\pi m_0^2} \int \frac{|\langle u^c_{\mathbf{k}} | P_x | u^v_{\mathbf{k}} \rangle|^2}{[E_c(k) - E_v(k)]^3} k\, dk\, d\theta, \tag{9}$$

with m_0 the free electron mass, although *ab initio* calculations might be necessary for accurate computation of r_0 depending on the material [61].

3.2. Influence of the tilt parameter

When computing the momentum matrix element present in equation (9), a dependence on t is only present on its x component as

$$P_x = \frac{m_0}{\hbar} \frac{\partial}{\partial k_x} \hat{\mathcal{H}}_d = \frac{m_0}{\hbar} \begin{bmatrix} t - 2k_x\alpha & -iv\eta \\ iv\eta & t + 2k_x\alpha \end{bmatrix}. \tag{10}$$

However, the diagonal terms proportional to t are canceled by the orthogonality relation of the two eigenvectors when $\langle u^c_{\mathbf{k}} | P_x | u^v_{\mathbf{k}} \rangle$ is computed. Explicitly, this term reads

$$e^{-i\theta} t \left[a^\dagger_+(k)\, a_-(k) + b^\dagger_+(k)\, b_-(k) \right] = 0, \tag{11}$$

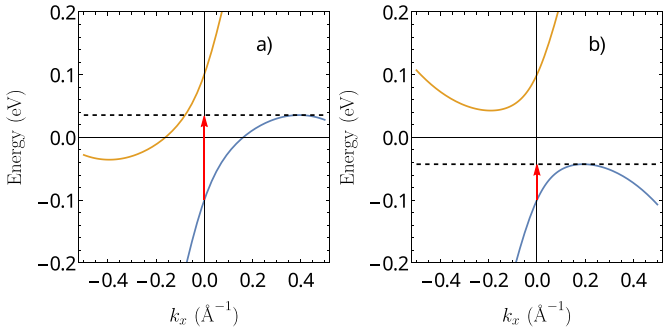

Figure 3. Band structure of the tilted model for two different values of the tilt parameter, $t = 1.1v$ (a) and $t = 0.83v$ (b). In each case we show the excitonic level (dashed lines) for different substrates, hBN (a) and quartz (b). The values chosen for t correspond to the onset of the excitonic instability for each case.

with $a_\pm$ and $b_\pm$ the normalized spinor components of the eigenvectors in equation (4), written generically as

$$|u_+(k,\theta)\rangle = \begin{bmatrix} a_+(k) \\ b_+(k)\, e^{i\theta} \end{bmatrix}, \quad |u_-(k,\theta)\rangle = \begin{bmatrix} a_-(k)\, e^{-i\theta} \\ b_-(k) \end{bmatrix}. \tag{12}$$

This cancellation, together with the fact that neither the difference of energy between the two bands nor the eigenvectors themselves depend on t, implies that the t parameter will not change the results obtained from solving the Bethe–Salpeter equation. As such, the obtained excitonic states will be independent of the tilt parameter t.

First considering the TMD encapsulated in hBN, the energies of first and second s-series states are, respectively, $E_{1s} = 134\,\text{meV}$ and $E_{2s} = 176\,\text{meV}$. When $t \approx 1.1v$, the top of the valence band crosses the excitonic level, as shown in figure 3(a). This marks the onset of the instability against the spontaneous formation of excitons. Although the system is a semi-metal for this value of the ratio t/v, the carrier density is still very small, indicating that screening is still weak and the long-range character of the electron–hole interaction should be preserved.

By changing the material by which the TMD is encapsulated, it is possible to tune the exciton binding energy. For instance, by replacing hBN by quartz (whose relative dielectric constant is 3.8 [62]), the energy of the $1s$ exciton is $E_{1s} = 56.6\,\text{meV}$. In this case, the onset of the excitonic instability happens for $t \approx 0.83v$, well into the semiconducting regime, as shown in figure 3(b). The fact that, for all $t \neq 0$, the gap is indirect, guarantees that the renormalization of the exciton binding energy and the dielectric function are small even for an arbitrarily small gap [41]. In figure 4, we plot the indirect bandgap of the system as a function of the tilt parameter t/v. As expected, when $t/v = 1$ the gap is closed. Additionally, the energy level of the vertical exciton $1s$ state for a quartz–encapsulated system is plotted in red, intersecting with the indirect bandgap line at $t/v \approx 0.898$.

In figure 5 we plot the absolute value squared of the first two s-series excitonic wave functions where the TMD has been

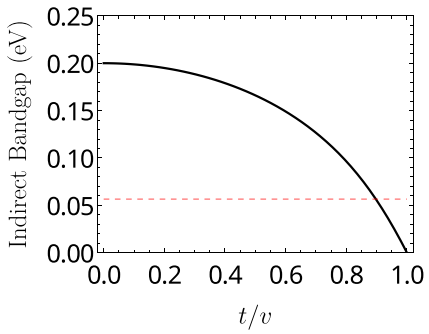

Figure 4. Indirect bandgap measured between the maximum of the valence band and the minimum of the conduction band from equation (3) as a function of the tilt parameter t/v. The red dashed line represents the energy of the vertical exciton $1s$ state in a quartz–encapsulated system.

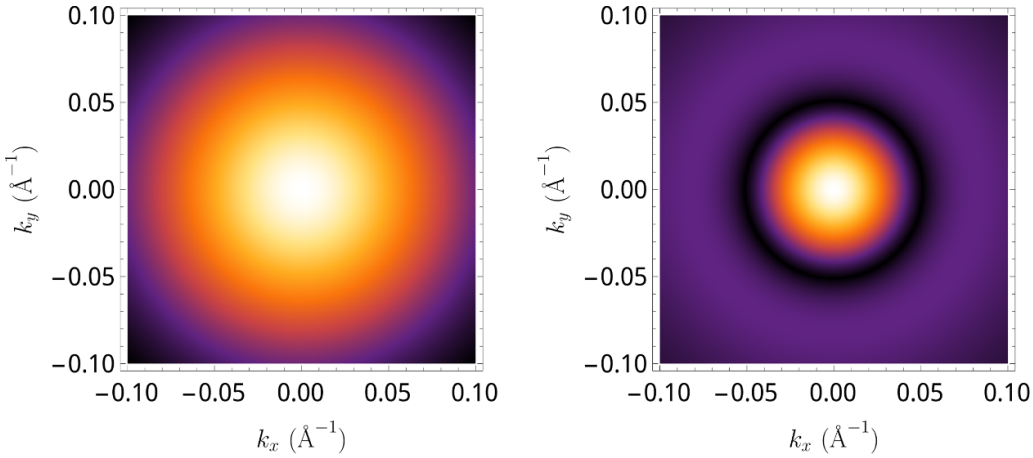

Figure 5. Absolute value squared of the wave functions of the two lowest energy excitonic s-series states centered at $k = 0$ considering the TMD encapsulated in quartz.

encapsulated in quartz. These plots are centered at $k = 0$ for a square region of side 20 Å^{-1}.

3.3. Excitonic conductivity

In the dipole approximation, and considering normal incidence, the optical conductivity is given by [53]

$$\sigma^{(1)}_{\alpha,\beta}(\hbar\omega) \propto \sum_n E_n \frac{\mathbf{\Omega}_{n,\alpha}\mathbf{\Omega}^*_{n,\beta}}{E_n - \hbar\omega - i\Gamma_n} + (\omega \to -\omega)^*, \quad (13)$$

where the sum over n represents the sum over excitonic states with energy E_n and wave function ψ_n, and Γ_n is a phenomenological broadening parameter considered to be n-dependent in a similar fashion as [56]. In equation (13), $\mathbf{\Omega}_{n,\alpha}$ is defined as

$$\mathbf{\Omega}_{n,\alpha} = \sum_{\mathbf{k}} \psi_n(\mathbf{k}) \langle u^v_{\mathbf{k}} | \mathbf{r}_\alpha | u^c_{\mathbf{k}} \rangle, \quad (14)$$

with $\langle u^v_{\mathbf{k}} | \mathbf{r}_\alpha | u^c_{\mathbf{k}} \rangle$ the interband dipole operator matrix element in the α direction, obtained using the relation

$$\langle u^v_{\mathbf{k}} | \mathbf{r}_\alpha | u^c_{\mathbf{k}} \rangle = \frac{\langle u^v_{\mathbf{k}} | [H, \mathbf{r}_\alpha] | u^c_{\mathbf{k}} \rangle}{E^v_k - E^c_k}. \quad (15)$$

Inserting this relation into equation (13), we then write the excitonic xx-conductivity as

$$\sigma^{(1)}_{xx}(\omega) = \frac{e^2}{4\,\pi^2 i\hbar} \sum_n \frac{E_n \left| \int \psi_n(\mathbf{k}) \frac{\langle u^v_{\mathbf{k}} | [H,x] | u^c_{\mathbf{k}} \rangle}{E^v_k - E^c_k} k\, dk\, d\theta \right|^2}{E_n - (\hbar\omega + i\Gamma_n)} + (\omega \to -\omega)^*. \quad (16)$$

The optical selection rules are directly obtained from the phase factors of the single particle states in equation (12) when the commutator $\langle u^v_{\mathbf{k}} | [H, \mathbf{r}_\alpha] | u^c_{\mathbf{k}} \rangle$ is explicitly expanded. Recalling equation (10), as well as the discussion regarding eigenvector orthogonality that followed, the allowed transitions are associated with states with angular momentum $\ell = 0$ (s-series states) and $\ell = \pm 2$ (d-series states). Explicitly, the commutator reads

$$\langle u^v_{\mathbf{k}} | [H,x] | u^c_{\mathbf{k}} \rangle = \mathcal{A}(k) + \mathcal{B}(k)\, e^{-2i\theta}, \quad (17)$$

with $\mathcal{A}(k)$ and $\mathcal{B}(k)$ the radial dependence of both the spinor components and the numerical parameters in the momentum

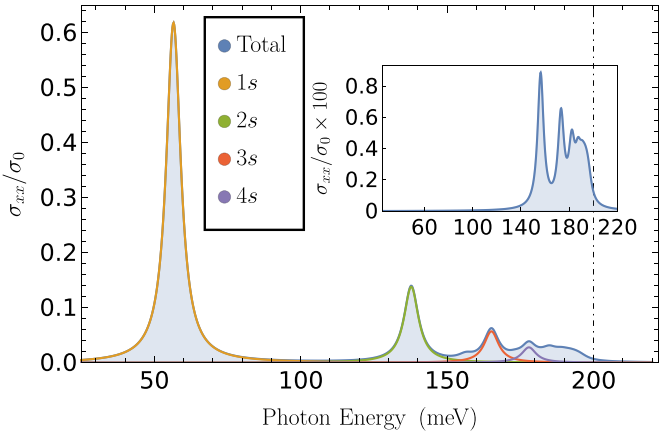

Figure 6. Real part of the excitonic xx-conductivity for a material described by a tilted Dirac Hamiltonian encapsulated in quartz with broadening parameter $\Gamma = 3\,\text{meV}$, and a $N = 450$ point Gauss–Legendre quadrature. First ten states of each excitonic series were considered for the total conductivity. Vertical dashed lines represent the bandgap of the system. The conductivity is given in units of the conductivity of monolayer graphene $\sigma_0 = e^2/4\hbar$. In the inset, we plot the contribution from only d-series states scaled by two orders of magnitude to improve readability and comparison of the relative intensity. The vertical dashed line representing the bandgap has been aligned by the same value in both the main plot and the inset.

matrix of equation (10). These two functions are then given by

$$\mathcal{A}(k) = -iv\eta a_+^\dagger(k) b_-(k) + k\alpha\left[b_+^\dagger(k) b_-(k) - a_+^\dagger(k) a_-(k)\right],$$
$$\mathcal{B}(k) = iv\eta b_+^\dagger(k) a_-(k) + k\alpha\left[b_+^\dagger(k) b_-(k) - a_+^\dagger(k) a_-(k)\right]. \tag{18}$$

To compare the oscillator strength of the two possible types of transitions, we compute the oscillator strength for d-series transitions as

$$|\mathbf{\Omega}_{n,d;x}|^2 = \left|\int \frac{f_{n;d}(k)\, e^{2i\theta}\mathcal{B}(k)\, e^{-2i\theta}}{E_k^v - E_k^c} k\, dk\, d\theta\right|^2, \tag{19}$$

where $f_{n;d}(k)$ is the excitonic radial wave function for d-series states. On the other hand, the oscillator strength for s-series transitions is given by

$$|\mathbf{\Omega}_{n,s;x}|^2 = \left|\int \frac{f_{n;s}(k)\,\mathcal{A}(k)}{E_k^v - E_k^c} k\, dk\, d\theta\right|^2, \tag{20}$$

where $f_{n;s}(k)$ is the excitonic radial wave function for s-series states. The first resonance for the $\ell = 2$ angular momentum series occurs at around 156 meV, and we obtain an oscillator strength around 2 orders of magnitude smaller than that of the s-series transitions closest to it.

In figure 6, we plot the real part of the excitonic xx-conductivity with a broadening parameter of $\Gamma = 3\,\text{meV}$. In its inset, the contribution from d-series states is also plotted, magnified by a factor of 100 as to improve comparison of the oscillator strengths of both types of transitions.

4. Conclusions

We studied the properties of excitons in Janus TMD monolayers modeled by a tilted massive Dirac Hamiltonian. We have shown that, as the tilt parameter increases, the band gap is continuously suppressed, whereas the maximum of the valence band and the minimum of the conduction band shift in opposite directions along the tilting axis, making the gap indirect. Notably, the exciton binding energies remain unchanged as the tilting is enhanced. This means that the (indirect) gap can be made smaller than the exciton binding, a situation that has been predicted to lead to an excitonic instability, and possibly the formation of an excitonic insulator phase.

Finally, we also considered the excitonic linear conductivity, discussing the optical selection rules for the system. With the model Hamiltonian considered, only states with angular momentum $\ell = 0$ or $|\ell| = 2$ can be excited, with the resonances associated with $\ell = 0$ transitions more than two orders of magnitude greater than those associated with $\ell = \pm 2$ transitions. As expected from the solutions of the Bethe–Salpeter equation, the excitonic linear conductivity was also fully independent of the tilt parameter, even when comparing light polarized in either the parallel or the perpendicular direction of the tilt axis. Importantly, the excitonic contribution to the conductivity is insensitive to the value of the tilting parameter t. As the system is pushed towards the excitonic instability by tuning t, one can expect $\sigma_{xx}(\omega)$ to remain unchanged until the system reaches the instability point, where $\sigma_{xx}(\omega)$ is expected to change abruptly, marking the onset of the phase change.

Data availability statement

All data that support the findings of this study are included within the article (and any supplementary files).

Acknowledgments

We acknowledge fruitful discussions with Joaquín Fernández-Rossier and Gonçalo Catarina. M F C M Q acknowledges the International Nanotechnology Laboratory (INL) and the Portuguese Foundation for Science and Technology (FCT) for the Quantum Portugal Initiative (QPI) Grant SFRH/BD/151114/2021. N M R P acknowledges support by the Portuguese Foundation for Science and Technology (FCT) in the framework of the Strategic Funding UIDB/04650/2020, COMPETE 2020, PORTUGAL 2020, FEDER, and FCT through Projects POCI-01-0145-FEDER-028114, POCI-01-0145-FEDER-02888 and PTDC/NANOPT/29265/2017, PTDC/FIS-MAC/2045/2021, EXPL/FIS-MAC/0953/2021, and from the European Commission through the Project Graphene Driven Revolutions in ICT and Beyond (Reference No. 881603, CORE 3).

ORCID iDs

M F C Martins Quintela https://orcid.org/0000-0002-0961-9235

A T Costa https://orcid.org/0000-0003-2899-6287
N M R Peres https://orcid.org/0000-0002-7928-8005

References

[1] Lu A-Y *et al* 2017 Janus monolayers of transition metal dichalcogenides *Nat. Nanotechnol.* **12** 744–9
[2] Zhang J *et al* 2017 Janus monolayer transition-metal dichalcogenides *ACS Nano* **11** 8192–8
[3] Riis-Jensen A C 2020 Computational studies of two-dimensional materials and heterostructures *PhD Thesis* Technical University of Denmark
[4] Zheng T *et al* 2021 Excitonic dynamics in Janus MoSSe and WSSe monolayers *Nano Lett.* **21** 931–7
[5] Tang X and Kou L 2022 2D Janus transition metal dichalcogenides: properties and applications *Phys. Status Solidi* b **259** 2100562
[6] Zhang C-G, Zhao D-D, Ji W-X, Zhang C-W and Wang P-J 2022 Monolayer NbNSe with high Fermi velocity and anisotropic properties *Phys. Status Solidi* b **259** 2100440
[7] Dong L, Lou J and Shenoy V B 2017 Large in-plane and vertical piezoelectricity in Janus transition metal dichalchogenides *ACS Nano* **11** 8242–8
[8] Liu J and Pantelides S T 2018 Mechanisms of pyroelectricity in three- and two-dimensional materials *Phys. Rev. Lett.* **120** 207602
[9] Hu T, Jia F, Zhao G, Wu J, Stroppa A and Ren W 2018 Intrinsic and anisotropic Rashba spin splitting in Janus transition-metal dichalcogenide monolayers *Phys. Rev.* B **97** 235404
[10] Jin H, Wang T, Gong Z-R, Long C and Dai Y 2018 Prediction of an extremely long exciton lifetime in a Janus-MoSTe monolayer *Nanoscale* **10** 19310–5
[11] Ma X, Wu X, Wang H and Wang Y 2018 A Janus MoSSe monolayer: a potential wide solar-spectrum water-splitting photocatalyst with a low carrier recombination rate *J. Mater. Chem.* A **6** 2295–301
[12] Jin C, Tang X, Tan X, Smith S C, Dai Y and Kou L 2019 A Janus MoSSe monolayer: a superior and strain-sensitive gas sensing material *J. Mater. Chem.* A **7** 1099–106
[13] Idrees M, Din H U, Ali R, Rehman G, Hussain T, Nguyen C V, Ahmad I and Amin B 2019 Optoelectronic and solar cell applications of Janus monolayers and their van der Waals heterostructures *Phys. Chem. Chem. Phys.* **21** 18612–21
[14] Berry M V 1984 Quantal phase factors accompanying adiabatic changes *Proc. R. Soc.* A **392** 45–57
[15] Xiao Di, Chang M-C and Niu Q 2010 Berry phase effects on electronic properties *Rev. Mod. Phys.* **82** 1959–2007
[16] Sodemann I and Fu L 2015 Quantum nonlinear Hall effect induced by Berry curvature dipole in time-reversal invariant materials *Phys. Rev. Lett.* **115** 216806
[17] Joseph N B, Roy S and Narayan A 2021 Tunable topology and Berry curvature dipole in transition metal dichalcogenide Janus monolayers *Mater. Res. Express* **8** 124001
[18] Du Z Z, Wang C M, Lu H-Z and Xie X C 2018 Band signatures for strong nonlinear Hall effect in bilayer WTe_2 *Phys. Rev. Lett.* **121** 266601
[19] Haastrup S *et al* 2018 The computational 2D materials database: high-throughput modeling and discovery of atomically thin crystals *2D Mater.* **5** 042002
[20] Zabolotskiy A D and Lozovik Y E 2016 Strain-induced pseudomagnetic field in the Dirac semimetal borophene *Phys. Rev.* B **94** 165403
[21] Verma S, Mawrie A and Ghosh T K 2017 Effect of electron-hole asymmetry on optical conductivity in 8-*pmmn* borophene *Phys. Rev.* B **96** 155418
[22] Sandoval-Santana J C, Ibarra-Sierra V G, Kunold A and Naumis G G 2020 Floquet spectrum for anisotropic and tilted Dirac materials under linearly polarized light at all field intensities *J. Appl. Phys.* **127** 234301
[23] Champo A E and Naumis G G 2019 Metal-insulator transition in 8-*pmmn* borophene under normal incidence of electromagnetic radiation *Phys. Rev.* B **99** 035415
[24] Herrera S A and Naumis G G 2019 Kubo conductivity for anisotropic tilted Dirac semimetals and its application to 8-*pmmn* borophene: role of frequency, temperature and scattering limits *Phys. Rev.* B **100** 195420
[25] Ogata M, Ozaki S and Matsuura H 2022 Anomalous spin transport properties of gapped Dirac electrons with tilting *J. Phys. Soc. Japan* **91** 023708
[26] Muechler L, Alexandradinata A, Neupert T and Car R 2016 Topological nonsymmorphic metals from band inversion *Phys. Rev.* X **6** 041069
[27] Li J, Xu T, Zhu G-B and Pan H 2020 Photoinduced anomalous Hall and nonlinear Hall effect in borophene *Solid State Commun.* **322** 114092
[28] Rostami H and Juričić V 2020 Probing quantum criticality using nonlinear Hall effect in a metallic Dirac system *Phys. Rev. Res.* **2** 013069
[29] Ohki D, Hirata M, Tani T, Kanoda K and Kobayashi A 2020 Chiral excitonic instability of two-dimensional tilted Dirac cones *Phys. Rev. Res.* **2** 033479
[30] Guan M-X, Wang E, You P-W, Sun J-T and Meng S 2021 Manipulating Weyl quasiparticles by orbital-selective photoexcitation in WTe_2 *Nat. Commun.* **12** 1885
[31] Winter S M, Riedl K and Valentí R 2017 Importance of spin–orbit coupling in layered organic salts *Phys. Rev.* B **95** 060404
[32] Osada T 2018 Topological insulator state due to finite spin–orbit interaction in an organic Dirac fermion system *J. Phys. Soc. Japan* **87** 075002
[33] Morimoto T and Nagaosa N 2016 Topological nature of nonlinear optical effects in solids *Sci. Adv.* **2** e1501524
[34] Gao Y and Ge B 2021 Second harmonic generation in Dirac/Weyl semimetals with broken tilt inversion symmetry *Opt. Express* **29** 6903–14
[35] Pardo V and Pickett W E 2009 Half-metallic semi-Dirac-point generated by quantum confinement in TiO_2/VO_2 nanostructures *Phys. Rev. Lett.* **102** 166803
[36] Huang H, Liu Z, Zhang H, Duan W and Vanderbilt D 2015 Emergence of a Chern-insulating state from a semi-Dirac dispersion *Phys. Rev.* B **92** 161115
[37] Saha K 2016 Photoinduced Chern insulating states in semi-Dirac materials *Phys. Rev.* B **94** 081103
[38] Chen J-N, Yang Y-Y, Zhou Y-L, Wu Y-J, Duan H-J, Deng M-X and Wang R-Q 2022 Photon-modulated linear and nonlinear anomalous Hall effects in type-II semi-Dirac semimetals *Phys. Rev.* B **105** 085124
[39] Zhang Y, van den Brink J, Felser C and Yan B 2018 Electrically tuneable nonlinear anomalous Hall effect in two-dimensional transition-metal dichalcogenides WTe_2 and $MoTe_2$ *2D Mater.* **5** 044001
[40] Mott N F 1961 The transition to the metallic state *Phil. Mag.* **6** 287–309
[41] Cloizeaux J D 1965 Exciton instability and crystallographic anomalies in semiconductors *J. Phys. Chem. Solids* **26** 259–66
[42] Kohn W 1967 Excitonic phases *Phys. Rev. Lett.* **19** 439–42
[43] Jérome D, Rice T M and Kohn W 1967 Excitonic insulator *Phys. Rev.* **158** 462–75
[44] Halperin B I and Rice T M 1968 The excitonic state at the semiconductor-semimetal transition *Solid State Physics* vol 21 (New York: Academic) pp 115–92
[45] Knox R S 1963 *Theory of Excitons* (*Solid State Physics Supplement*) 1st edn (New York: Academic)

[46] Du L, Li X, Lou W, Sullivan G, Chang K, Kono J and Du R-R 2017 Evidence for a topological excitonic insulator in InAs/GaSb bilayers *Nat. Commun.* **8** 1971
[47] Varsano D, Palummo M, Molinari E and Rontani M 2020 A monolayer transition-metal dichalcogenide as a topological excitonic insulator *Nat. Nanotechnol.* **15** 367–72
[48] Samaneh Ataei S, Varsano D, Molinari E and Rontani M 2021 Evidence of ideal excitonic insulator in bulk MoS_2 under pressure *Proc. Natl Acad. Sci.* **118** e2010110118
[49] Jia Y *et al* 2022 Evidence for a monolayer excitonic insulator *Nat. Phys.* **18** 87–93
[50] Sun B *et al* 2022 Evidence for equilibrium exciton condensation in monolayer WTe_2 *Nat. Phys.* **18** 94–99
[51] Shen S-Q 2012 *Topological Insulators* (Berlin: Springer)
[52] Taghizadeh A and Pedersen T G 2019 Nonlinear optical selection rules of excitons in monolayer transition metal dichalcogenides *Phys. Rev.* B **99** 235433
[53] Pedersen T G 2015 Intraband effects in excitonic second-harmonic generation *Phys. Rev.* B **92** 235432
[54] Cao T, Wu M and Louie S G 2018 Unifying optical selection rules for excitons in two dimensions: band topology and winding numbers *Phys. Rev. Lett.* **120** 087402
[55] Radha S K, Lambrecht W R L, Cunningham B, Grüning M, Pashov D and van Schilfgaarde M 2021 Optical response and band structure of $LiCoO_2$ including electron-hole interaction effects *Phys. Rev.* B **104** 115120
[56] Henriques J C G, Epstein I and Peres N M R 2022 Absorption and optical selection rules of tunable excitons in biased bilayer graphene *Phys. Rev.* B **105** 045411
[57] Martins Quintela M F C, Henriques J C G, Tenório L G M and Reis Peres N M M 2022 Theoretical methods for excitonic physics in two-dimensional materials *Phys. Status Solidi* b **259** 2200097
[58] Rytova S N 1967 The screened potential of a point charge in a thin film *Mosc. Phys. Bull.* **3** 30–37
[59] Keldysh L V 1979 Coulomb interaction in thin semiconductor and semimetal films *Sov. J. Exp. Theor. Phys. Lett.* **29** 658
[60] Li P and Appelbaum I 2019 Excitons without effective mass: biased bilayer graphene *Phys. Rev.* B **99** 035429
[61] Tian T, Scullion D, Hughes D, Li L H, Shih C-J, Coleman J, Chhowalla M and Santos E J G 2020 Electronic polarizability as the fundamental variable in the dielectric properties of two-dimensional materials *Nano Lett.* **20** 841–51
[62] Serway R A, Faughn J S and Moses C J 2003 *College Physics* vol 1 (Devon: Brooks/Cole)